The Astrophysical Journal, 874:69 (13pp), 2019 March 20 https://doi.org/10.3847/1538-4357/ab0a71

Chandra-HETGS Characterization of an Outflowing Wind in the Accreting Millisecond Pulsar IGR J17591–2342

Michael A. Nowak[1], Adamantia Paizis[2], Gaurava Kumar Jaisawal[3], Jérôme Chenevez[3], Sylvain Chaty[4], Francis Fortin[4], Jérôme Rodriguez[4], and Jörn Wilms[5]
[1] Physics Department, CB 1105, Washington University, One Brookings Drive, St. Louis, MO 63130-4899, USA; mnowak@physics.wustl.edu
[2] Istituto Nazionale di Astrofisica, INAF-IASF, Via Alfonso Corti 12, I-20133 Milano, Italy; adamantia.paizis@inaf.it
[3] National Space Institute, Technical University of Denmark, Elektrovej 327-328, DK-2800 Lyngby, Denmark; gaurava@space.dtu.dk, jerome@space.dtu.dk
[4] AIM, CEA, CNRS, Université Paris-Saclay, Université Paris-Diderot, Sorbonne Paris Cité, F-91191 Gif sur Yvette, France; chaty@cea.fr, francis.fortin@cea.fr, jrodriguez@cea.fr
[5] Dr. Karl Remeis-Observatory & ECAP, University of Erlangen-Nuremberg, Sternwartstr. 7, D-96049 Bamberg, Germany; joern.wilms@sternwarte.uni-erlangen.de
Received 2019 January 10; revised 2019 February 22; accepted 2019 February 24; published 2019 March 26

Abstract

An accreting millisecond X-ray pulsar, IGR J17591−2342 was discovered in 2018 August in scans of the Galactic bulge and center by the *International Gamma-Ray Astrophysics Laboratory* X-ray and gamma-ray observatory. It exhibited an unusual outburst profile with multiple peaks in the X-ray, as observed by several X-ray satellites over 3 months. Here we present observations of this source performed in the X-ray/gamma-ray and near-infrared domains and focus on a simultaneous observation performed with the *Chandra* High Energy Transmission Gratings Spectrometer (HETGS) and the *Neutron Star Interior Composition Explorer* (*NICER*). The HETGS provides high-resolution spectra of the Si edge region that yield clues as to the source's distance and reveal evidence (at 99.999% significance) of an outflow with a velocity of 2800 km s^{-1}. We demonstrate good agreement between the *NICER* and HETGS continua, provided that one properly accounts for the differing manners in which these instruments view the dust-scattering halo in the source's foreground. Unusually, we find a possible set of Ca lines in the HETGS spectra (with significances ranging from 97.0% to 99.7%). We hypothesize that IGR J17591−2342 is a neutron star low-mass X-ray binary at the distance of the Galactic bulge or beyond that may have formed from the collapse of a white dwarf system in a rare, calcium-rich Type Ib supernova explosion.

Key words: accretion, accretion disks – pulsars: general – stars: low-mass – stars: neutron – X-rays: binaries

1. Introduction

Accreting millisecond X-ray pulsars (AMXPs) are a peculiar subclass of neutron star (NS) low-mass X-ray binaries (LMXBs). In general, no X-ray pulsations are detected in classical NS LMXBs: the magnetic field of the NS is believed to be too faint ($\lesssim 10^9$ G) to channel the accreting matter—provided by the low-mass companion star—and it ends up being buried in the accretion flow, producing a "spotless" accretion on the NS surface. In some cases, however, an X-ray pulsation is detected; it can be hundreds of seconds (e.g., ∼120 s, spinning down to ∼180 s over 40 yr in the case of GX 1+4; see Jaisawal et al. 2018) down to the millisecond domain, in the range of 1.7–9.5 ms (e.g., Patruno & Watts 2012; Campana & Di Salvo 2018), the so-called AMXPs. Currently, 21 such systems are known (Campana & Di Salvo 2018). The fast pulsations are believed to be the result of long-lasting mass transfer from an evolved companion via Roche lobe overflow, resulting in a spin-up of the NS (the recycling scenario; Alpar et al. 1982). These sources are very important because they provide the evolutionary link between accreting LMXBs and rotation-powered millisecond radio pulsars (MSPs). Indeed, such a link has been recently observed in a few systems where a transition from the radio MSP phase (rotation-powered) to the X-ray AMXP phase (accretion-powered) has been detected (transitional MSP; Papitto 2016 and references therein).

The AMXP IGR J17591−2342 was discovered by the *International Gamma-Ray Astrophysics Laboratory* (*INTEGRAL*) during monitoring observations of the Galactic center (PI: J. Wilms) and bulge (PI: E. Kuulkers[6]). The source was detected in a 20–40 keV IBIS/ISGRI (15 keV—1 MeV; Lebrun et al. 2003) mosaic image spanning 2018 August 10–11 (MJD 58,340–58,341) at a significance of approximately 9σ with a positional uncertainty of 3′ (Ducci et al. 2018). Located at the rim of the field of view of the coaligned, smaller field-of-view instrument JEM-X (3–35 keV; Lund et al. 2003), IGR J17591−2342 was not detected in this lower-energy bandpass field.

Subsequent observations with the *Neil Gehrels Swift* satellite refined the position to within a 3.″6 uncertainty (90% confidence level) and gave a preliminary estimate of the source's absorbed 0.3–10 keV X-ray flux of $(2.6 \pm 0.2) \times 10^{-10}$ erg cm^{-2} s^{-1} (Bozzo et al. 2018). The spectrum was consistent with a highly absorbed power law ($N_{\rm H} = (4.2 \pm 0.8) \times 10^{22}$ cm^{-2}, $\Gamma = 1.7 \pm 0.3$). Optical follow-up observations did not definitively reveal any counterpart within the *Swift* error circle (Russell & Lewis 2018); however, radio observations showed a counterpart with a flux of 1.09 ± 0.02 mJy at $\alpha_{\rm J2000.0} = 17{:}59{:}02.86$, $\delta_{\rm J2000.0} = -23{:}43{:}08.0$ (0.″6 uncertainty), which is within 2.″1 of the *Swift* position (Russell et al. 2018a).

Joint *Neutron Star Interior Composition Explorer* (*NICER*)/*NuSTAR* observations demonstrated that this radio and X-ray source was in fact an AMXP with a spin frequency of 527 Hz and an 8.8 hr orbital period with a likely companion mass $>0.42\,M_\odot$ (Ferrigno et al. 2018; Sanna et al. 2018). The pulsar spin was detected in both instruments. The 3–30 keV *NuSTAR* absorbed flux was 4.2×10^{-10} erg cm^{-2} s^{-1}, and the extrapolated 0.1–10 keV *NICER* flux was 1.3×10^{-10} erg cm^{-2} s^{-1}. It was further noted that the radio flux reported by Russell et al. (2018a) was approximately three times larger than that for

[6] http://integral.esac.esa.int/BULGE/

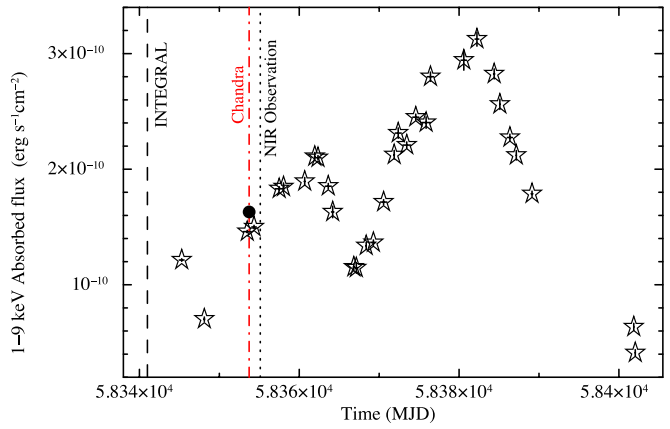

Figure 1. Light curve showing the absorbed 1–9 keV flux as determined by *NICER* observations (observation IDs 1200310101–1200310137). The times of the *INTEGRAL* discovery and our *Chandra* and NIR observations are also highlighted.

other observed AMXPs (see Tudor et al. 2017). Near-infrared (NIR) observations with the High Acuity Wide-field K-band Imager (HAWK-I) on the Very Large Telescope (VLT) further refined the position of IGR J17591−2342 to $\alpha_{J2000.0} =$ 17:59:02.87, $\delta_{J2000.0} = -23{:}43{:}08.2$ (0.″03 uncertainty; Shaw et al. 2018). The source was found to be faint in the NIR ($H = 19.56 \pm 0.07$ mag and $Ks = 18.37 \pm 0.07$ mag; Shaw et al. 2018; see also Section 2.4 below).

Starting at 2018 August 23, UTC 17:53 (MJD 58,353.74), we used the *Chandra X-ray Observatory* (Weisskopf et al. 2002) to perform a 20 ks long target-of-opportunity observation of IGR J17591−2342 employing the High Energy Transmission Gratings Spectrometer (HETGS; Canizares et al. 2005). As we have previously reported (Nowak et al. 2018; and see Section 2.1 below), our best determined position for IGR J17591−2342 is $\alpha_{J2000.0} =$ 17:59:02.83, $\delta_{J2000.0} = -23{:}43{:}08.0$ (0.″6 accuracy, 90% confidence limit). This position is consistent with the radio, NIR, and *Swift* determined positions (see Figure 3, Section 2.4 below).

Bracketing the times of our *Chandra* observations, proprietary deep *INTEGRAL* target-of-opportunity observations (August 17–19 and August 25–27, MJD 58,347–58,349 and 58,355–58,357, PI: Tsygankov; Kuiper et al. 2018) significantly detected the source up to 150 keV. The source exhibited a power-law spectrum with $\Gamma = 1.92 \pm 0.05$ in the second observation period, and its 1.9 ms pulsation was detected in the 20–150 keV band at 5.2σ (Kuiper et al. 2018).

An examination of archival *Neil Gehrels Swift* data showed that the initial brightening of IGR J17591−2342 occurred as early as 2018 July 22 (MJD 58,321) and peaked on 2018 July 25, predating the *INTEGRAL* discovery (Krimm 2018). Further *INTEGRAL* observations post–initial discovery showed a rebrightening of the source on 2018 August 30–31 (Kuiper et al. 2018; Sanchez-Fernandez et al. 2018). In Figure 1, we show the IGR J17591−2342 light curve for the absorbed 1–9 keV flux as determined by our analyses of *NICER* (Gendreau et al. 2016) observations (observation IDs 12000310101–1200310137; see Sections 2.2 and 3.4 below). The two peaks shown in Figure 1 occur past at least one earlier peak in the light curve (Krimm 2018), indicating a complex light curve. (The degree to which there is further substructure in the light curve over the July/August time frame is difficult to assess, owing to the disparate bandpasses of the various instruments with which IGR J17591−2342 was observed.)

IGR J17591−2342 is the 22nd member of the AMXP class. A high-resolution X-ray spectroscopic characterization of this system and its surrounding matter may yield insights as to the evolution of millisecond pulsars from their accreting LMXB progenitors. In this paper, we discuss in detail the *Chandra*-HETGS spectra referenced by Nowak et al. (2018). We present evidence of an ionized outflow with a velocity of order 1% the speed of light and attempt to discern local and interstellar absorption. Taking the *NICER* observations used to create the light curve in Figure 1, we model the spectra that were strictly simultaneous with our *Chandra* observation and discuss the differences in the model fits that are related to the different fields of view of these two instruments. We use *INTEGRAL* observations to discuss the spectra of IGR J17591−2342 above 10 keV. We also present new NIR observations and discuss their implications.

2. Observations

Here we describe observations of IGR J17591−2342 performed in several different energy bands with a variety of instruments. Although the primary discovery was obtained by *INTEGRAL* (Section 1), our main focus will be observations obtained with *Chandra* (Section 2.1) and the *NICER* (Section 2.2) observatories. After describing the observations performed with *Chandra* and *NICER*, we briefly describe observations obtained with *INTEGRAL* (Section 2.3) and discuss our follow-up optical and IR observations (Section 2.4).

2.1. Chandra-*HETGS Observations*

The HETGS consists of two sets of gratings, the high-energy gratings (HEGs, with bandpass ≈0.7–9 keV and spectral resolution $E/\Delta E \approx 1\,300$ at 1 keV) and the medium-energy gratings (MEGs, with bandpass ≈0.5–8 keV and spectral resolution $E/\Delta E \approx 700$ at 1 keV), each of which disperses spectra into positive and negative orders. Here we consider only ±first-order spectra of the HEGs and MEGs. There are too few counts to produce usable spectra from the higher spectral orders, while the undispersed zeroth-order spectra suffer from pileup. The first-order spectra do not suffer from pileup, as the peak pileup fraction (in MEG −1 order near 3.8 keV, where the count rate peaks at ≈0.13 counts s^{-1} $Å^{-1}$) is $\lesssim$0.5% and is significantly less for most other orders and wavelengths (see Hanke et al. 2009).

Our 20 ks *Chandra* data were processed using the suite of analysis scripts available as part of the Transmission Gratings Catalog (Huenemoerder et al. 2011), running tools from `CIAO v. 4.10` utilizing *Chandra* Calibration Database v. 4.7.8. The location of the center of the point source's zeroth-order image was determined by intersecting the dispersion arms via the `findzo` tool. This is the position reported by Nowak et al. (2018). Its 0.″6 accuracy (90% confidence) is that of the *Chandra* aspect solution when no other sources are within the field of view to further refine the astrometry.

Events within a 16 pixel radius of the above position were were assigned to zeroth order. This position also defined the location of the dispersed HEG and MEG spectra. Any events that fell within ±16 pixels of the cross-dispersion direction of either the HEG or MEG spectra were assigned to that grating arm using the `tg_create_mask` tool. Spectra were then

created with events that fell within ±3 pixels of the cross-dispersion direction of the HEG and MEG arm locations (`tg_extract`) and assigned to a given spectral order with `tg_resolve_events` using the default settings. Spectral response matrices were created with the standard tools (`fullgarf` and `mkgrmf`).

2.2. NICER *Observations*

A series of observations with *NICER* were performed throughout the outburst of IGR J17591−2342 (see Sanna et al. 2018 and Figure 1). A total of 2.64 ks were strictly simultaneous with our 20 ks *Chandra*-HETGS observations. We consider only these data for purposes of spectral fitting. There are more *NICER* pointings, likely having a very similar spectral shape and flux, from periods shortly before or after the data sets that we consider. Our spectra, however, are already near the limits of the current understanding of systematic uncertainties in the *NICER* instrumental responses; therefore, inclusion of additional data would not improve our understanding of the *NICER* spectra.

The spectra were extracted using the *NICER* tools available in the `Heasoft v6.25` package, using calibration products current as of the release of 2018 November 5. The response files were `ni_xrcall_onaxis_v1.02.arf` and `nicer_v1.02.rmf`, which we obtained directly from the *NICER* instrument team. We created a background file from *NICER* observations (with 66 ks of effective exposure) of a blank sky field previously observed by the *Rossi X-ray Timing Explorer*[7] (*RXTE*). In all of the fits described below, rather than include a scaled version of these data as part of the spectral fit (i.e., "background subtraction," even though what one is doing in ISIS is essentially adding these scaled background data to the model fits and comparing to the total observed data), we model the background spectra with a power law (with energy index $\Gamma \approx 0.78 \pm 0.02$) and a broad Gaussian feature centered on an energy of (1.73 ± 0.07) keV with width $\sigma \approx (0.3 \pm 0.1)$ keV. This model is fit to the background data while simultaneously incorporating it into the source data model (without folding it through the spectral response and appropriately scaling it for the ≈0.04 relative exposure time of the source and background).

We bin the *NICER* spectra by a minimum of three spectral channels between 1 and 6 keV and four spectral channels between 6 and 9 keV. This approach ensures that our binning is approximately half-width at half-maximum of the *NICER* spectral resolution (as determined from empirical measurements of δ functions forward-folded through the *NICER* spectral response). Furthermore, we also impose a signal-to-noise minimum of 4; however, this latter criterion only affects the binning of the last few channels in the 8–9 keV range.

2.3. INTEGRAL *Observations*

In order to better understand the long-term behavior of IGR J17591−2342 at energies above 10 keV, we use *INTEGRAL* (Winkler et al. 2003, 2011) to study its high-energy spectra. We analyzed all of the available IBIS/ISGRI data of the monitoring observations[8] starting from 2018 July 1 (MJD 58,300; i.e., prior to the 2018 July 22 detection with archival data by Krimm 2018) up to 2018 October 23 (MJD 58,414). Pointings ("science windows" in *INTEGRAL* parlance) that had the source within the IBIS/ISGRI field of view (<15°) and with integrated good times >1000 s were used. This resulted in a total of 468 pointings of about 1 ks each (none of which were strictly simultaneous with our *Chandra* data). We analyzed the data using the Off-line Scientific Analysis version 11 and the latest instrument characteristic files (2018 November).

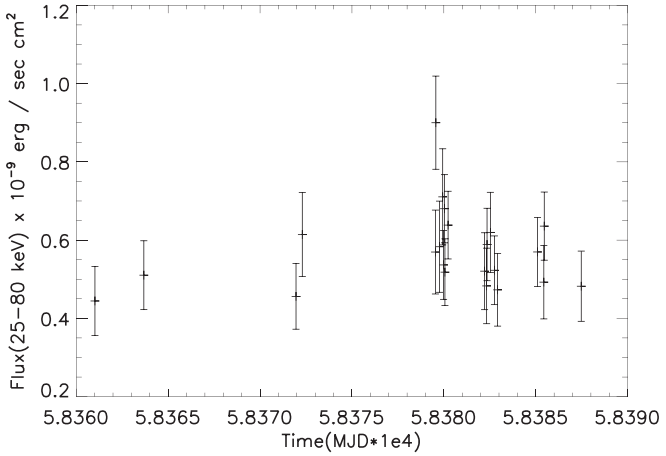

Figure 2. The IBIS/ISGRI 25–80 keV light curve of the hard X-ray brightest part of the outburst of IGR J17591−2342 (single pointing detections).

We detected IGR J17591−2342 in 22 pointings in the 25–80 keV band. In all of these pointings, the source was within ∼9° from the center of the field of view. Figure 2 shows the light curve when the source is detected at a pointing level. As can be seen with respect to Figure 1, the detections overlap with the highest-intensity periods from the *NICER* observations. The 25–80 keV source flux was obtained using a $\Gamma = 2$ power-law spectrum (see Section 3.1).

2.4. Optical/IR *Observations*

For optical follow-up, we triggered optical-to-infrared observations of IGR J17591−2342 at the European Organisation for Astronomical Research in the Southern Hemisphere (ESO) using the VLT X-shooter instrument, a large-band UVB-to-NIR spectrograph mounted on the UT2 Cassegrain focus (Vernet et al. 2011).

We obtained an *I*-band acquisition image on 25 August 2018, UTC 03h30 (exposure time 120 s). Figure 3 shows this finding chart of IGR J17591−2342 in the *I* band, as acquired by X-shooter, indicating the *Swift*-XRT, *Chandra*, ATCA, and VLT/HAWK-I localization circles referenced in Section 1. From the image, we derive a lower limit for the *I* magnitude of the counterpart of the X-ray source of $I \geqslant 24.7 \pm 0.6$ mag (Johnson filter, magnitude of the source at 3σ above the sky noise). The uncertainty on the determined magnitude is rather large because we used a mean zero-point to flux-calibrate the photometry. This value in the *I* band is consistent with the *H* and *Ks* values obtained with HAWK-I observations (Shaw et al. 2018).

We also obtained NIR spectra on 25 August 2018, UT03h33–04h37 (exposure time of 64 m, with airmass between 1.346 and 1.836), that we analyzed by performing a standard reduction using the `esoreflex` pipeline (Freudling et al. 2013). We detect a very faint spectrum (S/N ∼ 3.2 at the maximum of the whole band coverage), as expected for a faint

[7] Field number six of eight blank sky fields that were previously used for *RXTE* calibration (Jahoda et al. 1996).

[8] Galactic center (PI: J. Wilms) and bulge (PI: E. Kuulkers).

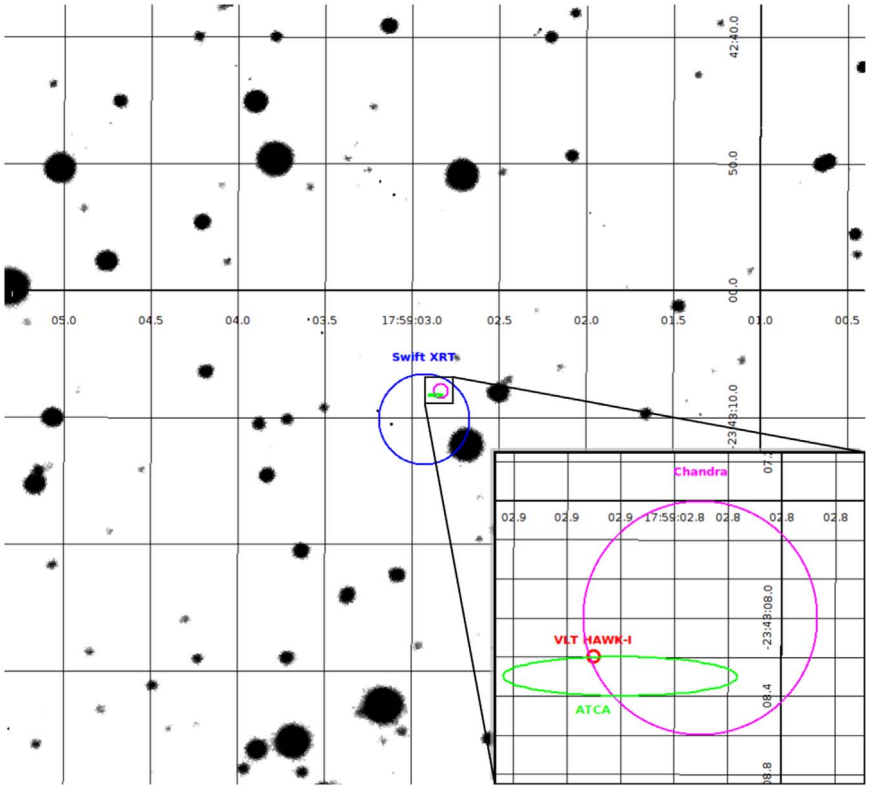

Figure 3. Finding chart of IGR J17591−2342 in the *I* band, as acquired by X-shooter, indicating the *Swift*-XRT, *Chandra*, ATCA, and VLT/HAWK-I localization circles.

source with the *I*-, *H*-, and *Ks*-band values discussed above. By flux-calibrating the faint spectrum, we find $F_\nu < 0.12$ mJy at the *K*-band wavelength of 2.2 μm (i.e., corresponding to $K > 16.8$ mag). By applying a median filter, we detect a faint continuum signal at the level of $F_\nu = 0.025$ mJy (i.e., $K = 18.6$). Both measurements are consistent with the *Ks* value obtained with HAWK-I observations.

We point out here that, in the absence of a detection of variability of the NIR candidate counterpart, we cannot unambiguously associate either the candidate counterpart claimed by Shaw et al. (2018) or the faint spectrum we detected with X-shooter with the variable X-ray source.

For the value of the equivalent neutral absorption column, $N_{\rm H} = (4.9 \pm 0.2) \times 10^{22}\,{\rm cm}^{-2}$, that we originally reported (Nowak et al. 2018; where we used the absorption model, cross sections, and interstellar medium (ISM) abundances discussed by Wilms et al. 2000), the corresponding *V*-band absorption is $Av \approx 24.6$ mag (using the relationship between equivalent neutral column and *V*-band absorption given by Predehl & Schmitt 1995; although, see our more detailed discussions of absorption modeling below), and the *K*-band absorption is $Ak \approx 2.77$ mag (using Fitzpatrick 1999).

The $I-K$ color value being greater than at least 6 mag suggests a late-spectral-type companion star, located at the distance of the Galactic bulge.

3. Spectral Fits

3.1. Hard X-Ray Continuum Fits

We first consider the IBIS/ISGRI spectra obtained from the average of the 22 pointings discussed above (i.e., the observations represented in the light curve shown in Figure 2). We fit these spectra with XSPEC v12.9.1 (Arnaud 1996) using a power law and found a spectrum with $\Gamma = 2.0 \pm 0.2$ (reduced $\chi^2 = 1.29$, 10 degrees of freedom). These *INTEGRAL* observations extend the bandpass beyond the ≈70 keV upper limit of the *NuSTAR* -observations, and here we find that IGR J17591−2342 is detected up to about 110 keV with no improvement obtained with the addition of a cutoff, even going out to ≈200 keV (Figure 4, top panel).

We selected five pointings for which IGR J17591−2342 was both bright (second peak from Figure 1, between MJD 58,380 and 58,383) and within the JEM-X fully coded field of view (where the detection significance is maximum, <3°). This selection resulted in a subsample of five science windows (IDs: 200100250010, 200100340010, 200200250010, 200200330010, and 200200340010). The simultaneous IBIS/ISGRI and JEM-X spectra of the five average pointings (Figure 4, bottom panel) resulted in a best-fit (reduced $\chi^2 = 0.66$, 19 degrees of freedom) power-law spectrum with $\Gamma = 1.8 \pm 0.2$ and frozen neutral hydrogen $N_{\rm H} = 3.3 \times 10^{22}\,{\rm cm}^{-2}$ (taken from model E in Table 3, as discussed below in Section 3.2). Again, no cutoff is required within the *INTEGRAL* band. The average absorbed fluxes are $F_{25-80\,{\rm keV}} = 4.7 \times 10^{-10}$, $F_{3-25\,{\rm keV}} = 5.4 \times 10^{-10}$, and $F_{1-9\,{\rm keV}} = 2.8 \times 10^{-10}\,{\rm erg\,cm^{-2}\,s^{-1}}$. These values are compatible with the *NICER* fluxes shown in Figure 1. Assuming a distance of 8 kpc, they correspond to luminosities of $L_{25-80\,{\rm keV}} = 3.6 \times 10^{36}$, $L_{3-25\,{\rm keV}} = 4.1 \times 10^{36}$, and $L_{1-9\,{\rm keV}} = 2.1 \times 10^{36}\,{\rm erg\,s^{-1}}$.

A deeper analysis of the *INTEGRAL* data (mosaicking detections, spectral variability, and timing) is beyond the scope of this paper.

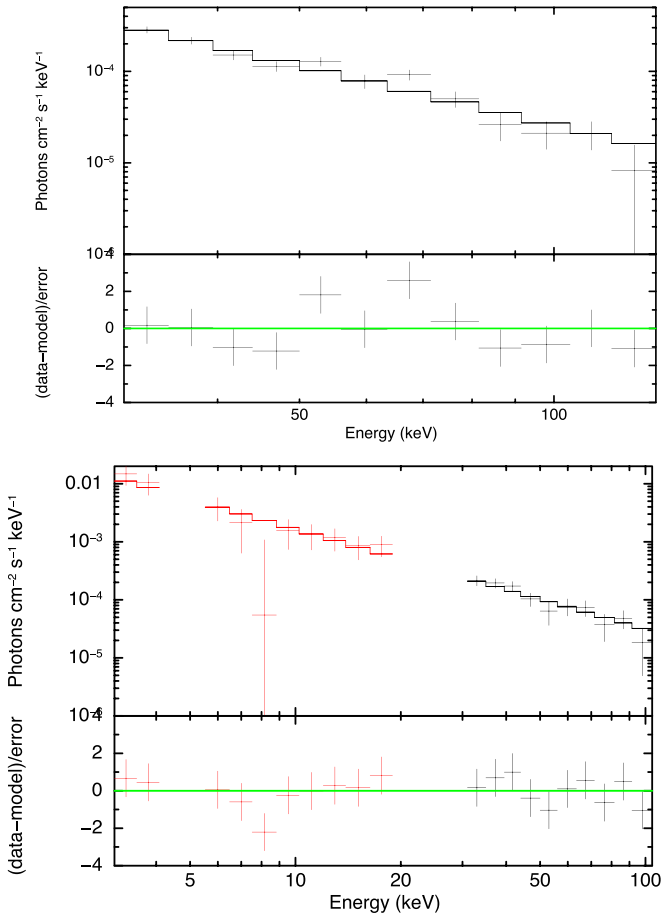

Figure 4. *INTEGRAL* spectra of IGR J17591−2342. Top panel: IBIS/ISGRI average spectrum and best fit of the data points shown in Figure 2 (effective exposure ∼24 ks). Bottom panel: simultaneous JEM-X (red) and IBIS/ISGRI (black) spectrum and best fit of five pointings with the source within the JEM-X fully coded field of view (effective exposure ∼6 ks with IBIS/ISGRI and ∼8 ks with JEM-X). See text.

3.2. Soft X-Ray Continuum and Line Fits

All further analyses presented below were performed with the `Interactive Spectral Interpretation System` (`ISIS`; Houck & Denicola 2000). In order to increase the signal-to-noise ratio of our spectra, we combine the positive and negative first-order HEG and MEG spectra using the `ISIS` functions `match_data set_grids` (to match the HEG wavelength grid to that of MEG) and `combine_data sets`.[9] We limit the energy range to 1–9 keV but do not further bin the data, and we use Cash (1979) statistics in the fits so as to facilitate the spectral line search without biasing against absorption lines (see below).

We use a continuum model similar to the one Sanna et al. (2018) employed to fit joint *NICER*/*NuSTAR* data of IGR J17591−2342, specifically an absorbed (`tbvarabs`; Wilms et al. 2000, where we have also adopted the atomic cross sections and ISM abundances discussed in that work) blackbody (`bbodyrad`) plus Comptonization (`nthcomp`; Życki et al. 1999) spectrum. Lacking simultaneous data above 9 keV, we do not have good leverage on some of the Comptonization parameters, so for all models, we fix the coronal temperature to the 22 keV value found by Sanna et al. (2018) such that we can more readily compare to their findings. Our results in the 1–9 keV band are not sensitive to the coronal temperature; however, we note that a 22 keV coronal temperature would imply a spectral curvature in the 50–150 keV band that we do not see in the *INTEGRAL* spectra shown in Figure 4. The remaining `nthcomp` parameters are the normalization ($N_{\rm nc}$), Compton power-law photon index ($\Gamma_{\rm nc}$), and seed photon temperature ($kT_{\rm nc}$). The latter is tied to the blackbody temperature. The remaining `bbodyrad` parameter is its normalization, $N_{\rm bb}$, which nominally corresponds to $R^2_{\rm km}/D^2_{10\,\rm kpc}$, where $R_{\rm km}$ is the source radius in km, and $D_{10\,\rm kpc}$ is the source distance in units of 10 kpc.

We include one other component in our model that is not found in the *NICER* modeling of Sanna et al. (2018), namely, a dust-scattering component using the `dustscat` model (Baganoff et al. 2003). This component accounts for the scattering of soft X-rays out of our line of sight due to dust grains (see the discussion of Corrales et al. 2016). Taking this effect into account is important for the high spatial resolution measurements done with *Chandra*, which resolve IGR J17591−2342 into a point source and an arcminute-sized dust-scattering halo. In contrast, as we further discuss below, the halo emission is included in the overall *NICER* spectrum owing to the arcminute-scale-resolution line of sight provided by this instrument. Following Nowak et al. (2012), in our *Chandra* analysis, we therefore tie the halo optical depth to a value of $\tau_{\rm scat} = 0.324(N_{\rm H}/10^{22}\,{\rm cm}^{-2})$, where $N_{\rm H}$ is the equivalent neutral column obtained from the `tbvarabs` model. The dust halo size relative to the instrumental point-spread function (PSF) is frozen at $H_{\rm size} = 200$ (i.e., nearly all scattered photons are lost).

Our continuum model with the dust-scattering halo describes the HETG spectra well (Cash statistic = 2048.6 for 2200 degrees of freedom), with a fitted equivalent neutral hydrogen column of $N_{\rm H} = (4.4 \pm 0.2) \times 10^{22}\,{\rm cm}^{-2}$. The modeled 1–9 keV absorbed flux is $1.58 \times 10^{-10}\,{\rm erg\,cm^{-2}\,s^{-1}}$. (All implied 1–9 keV absorbed fluxes for the models discussed below fall within a few percent of this value for the *Chandra*-HETGS spectra.) Assuming a distance of 8 kpc, this translates to an absorbed, isotropic luminosity in the 1–9 keV band of $1.21 \times 10^{36}\,{\rm erg\,cm^{-2}\,s^{-1}}$.

There are a number of prominent, narrow residuals in the spectra, especially near the Si edge region. To assess these residuals, we perform a "blind line search" (see the description of this functionality in Nowak 2017). We write our model (using `ISIS` notation) as follows:

```
tbvarabs * powerlaw * exp
 ×(lines/bin_width_en) + 0 * (constant + ...),
```
(1)

where `tbvarabs` is the Wilms et al. (2000) absorption model, `powerlaw` is the standard function with photon energy index Γ, `exp` is an exponential function, and `bin_width_en` is a function that returns the width of a data spectral bin in keV. The function `lines` is defined within the search script and returns a sum of standard `Gaussian` fit functions, which, as defined in `ISIS` or `XSPEC`, are line profiles integrated within each data bin. It is for this latter reason that we divide by the

[9] The `combine_data sets` function essentially adds together the product of exposure, effective area, and response function for each individual observation within the standard forward-folding equation (Davis 2001) while also properly combining the background. It has been well vetted via comparisons against standard `Heasoft` and `CIAO` functions for combining spectral responses and backgrounds.

Table 1
Results of Blind Line Search

E_{obs} (keV)	ΔC	EW (eV)	Order	ID	z
1.0088	−12.8	98	1	⋯	⋯
1.6949	−9.3	−2.3	3	⋯	⋯
1.7349	−7.5	−2.1	9	Si Kα	0.003
1.8481	−8.4	−3.2	6	Si near edge	⋯
1.8825	−23.3	−4.3	0	Si XIIIr	−0.009
2.2181	−8.4	−4.2	4	Si XIIIb	−0.016
3.4727	−8.2	5.3	7	⋯	⋯
3.6865	−9.3	−5.6	2	Ca Kα	0.0004
3.8447	−8.3	6.1	5	Ca XIXi	0.010
3.8963	−7.3	−6.4	10	Ca XIXr	0.016
4.2955	−7.9	4.8	8	Ca XXa	0.044

Note. Results from a blind search to the unbinned, combined *Chandra*-HETG spectra, using a model consisting of an absorbed/scattered Comptonized spectrum. The columns give the fitted energy of the line, the change in Cash statistic when including the line, the line equivalent width (negative values are absorption, positive are emission), the order in which the lines were added (numbers 0–10), a potential line ID, and an implied redshift (negative values for blueshifts) if this ID is correct.

data bin widths, so that any rebinning of the data will not strongly affect the fit parameters. We multiply the continuum by line functions within an exponential to ensure that the model never yields negative counts and so that it can smoothly pass from absorption to emission lines. The (multiple) `constant` functions (multiplied by zero so as not to add to the continuum) are used as "dummy parameters" to allow us to transform the parameters of the `Gaussian` line functions. Rather than fit a line amplitude, we instead fit a parameter closer to line equivalent width. Further, as a line becomes significantly more absorbed, we increase its equivalent width by increasing the line width, rather than increasing the magnitude of the line amplitude. Since the data are not good enough to distinguish between being on the damping wings of the equivalent width curve of growth and a true increase in line width, we find that increasing the line width is numerically more stable. We limit all line widths to lie in the range of values $\sigma = 0.1$–20 eV.

In the line search procedure, we add an additional `Gaussian` function to the `lines` function, and, while holding the continuum and any previously detected lines fixed, we fit the parameters of this added line feature, allowing its amplitude, width, and energy (within a limited range) to be free parameters. We store the change in fit statistics and the parameters of the fitted line. We scan along the full energy range of the spectra in this manner. The 10 features with the largest change in fit statistic are then individually refit, now with both the continuum parameters and previous line fits allowed to vary. The feature leading to the largest improvement in fit statistic is then added to the model, and the scan is repeated. (At this stage, no error bars are determined for the line fits.)

Results for the 11 most significant features found by this method are presented in Table 1. Possible line identifications are also presented, along with the line redshifts if these identifications are in fact correct. These features were found in fits to the combined spectra; however, we visually inspected the combined fits applied to the spectra from the individual grating arms, as well as the spectra for just the combination of the HEG spectra and just the combination of the MEG spectra. The fitted features were consistent with these individual spectra, albeit with noisier statistics. None of the features appeared to be the result of a single spectrum or a single combination of spectra, as might be the case for an interloping faint source coincident with one grating arm or an unmodeled response feature limited to a subset of the arms.

Several significant features are found near the location of the expected Si absorption K edge, so we include these in subsequent models, constraining the line energies to lie within a 10 eV interval and have widths $\sigma < 10$ eV. The possible blueshifted Si XIII Lyα feature (see Hell et al. 2016 for the most recent measurements of its energy) is fairly significant, so we include it in all subsequent fits and further add Si XIII β and γ lines tied to the same blueshift and relative line width. Likewise, we include both the Si Kα line at 1.7349 keV (whether this is a real feature or an unmodeled component in the HETG response function) and the 1.848 keV feature near the Si edge (see discussion below). Although we have no good identification for the absorption feature near 1.695 keV, its presence may affect our models of the Si edge. We also include this feature in all subsequent models.

The possible presence of Ca features is somewhat unusual, but many of these features are formally more statistically significant than, e.g., the possible Si Kα absorption line. Given that they may provide some information about the nature of an evolved companion, we include them in all subsequent fits, constraining their line energies to lie within a 50 eV interval and have widths $\sigma < 20$ eV. They do not strongly influence any of the continuum or absorption parameters, as verified by Markov chain Monte Carlo (MCMC) error contours for all models and parameters discussed below. We do not attempt to tie these features to a single common Doppler shift.

Lacking any plausible identification for the 1.009 or 3.47 keV features, we do not include them in subsequent models. The former feature consists of only a few events in a very faint portion of the observed spectrum (hence its large equivalent width, despite being only a few detected events). The latter feature does not strongly influence the remaining fit parameters.

The above model fits the data well, with a Cash statistic of 1963.0 for 2172 degrees of freedom; however, it requires a fitted equivalent neutral column of $N_{\rm H} = (5.1^{+0.3}_{-0.1}) \times 10^{22}$ cm^{-2}. This value is somewhat larger than the $N_{\rm H} = (3.6 \pm 1.1)$–$(4.4 \pm 0.3) \times 10^{22}$ cm^{-2} values found by Sanna et al. (2018; *Swift*/*NICER*/ *NuSTAR*/*INTEGRAL*) and Russell et al. (2018b; *Swift*), respectively. Our higher equivalent neutral column value is in part driven by the need to describe the complexities of the Si K-edge region, as well as possibly also by differences in the abundance sets used. We consider this region further in Section 3.3 below.

3.3. Si Edge Region Models

Recently, Schulz et al. (2016) published a *Chandra*-HETGS study of the Si K-edge region of Galactic X-ray binaries with (continuum-) fitted equivalent neutral columns in the range of $N_{\rm H} \approx (1$–$6) \times 10^{22}$ cm^{-2}. Among the conclusions of this survey are that (1) the absorption model of Wilms et al. (2000), when using their adopted ISM abundances, underpredicts the depth of the Si K edge; (2) the edge itself is complex; (3) there is often a near-edge absorption feature at $\approx$1.849 keV that, even in a single source, appears to have a

variable equivalent width that is loosely correlated with fitted $N_{\rm H}$; and (4) there is often an Si XIII absorption feature, also with variable equivalent width, with an even weaker correlation with fitted $N_{\rm H}$. The variability of the latter two features indicates that for many of the 11 X-ray binaries included in the survey of Schulz et al. (2016), some fraction of the observed absorption is local to the system, as opposed to being more broadly distributed throughout the ISM.

The near-edge and Si XIII features are already accounted for in our models. The energy of the near-edge feature is consistent with the values found by Schulz et al. (2016); therefore, this feature is likely "at rest" relative to its expected energy. On the other hand, we do not find Si XIII at rest but instead find a blueshifted velocity of $\approx$2800 km s^{-1} with $\sigma \approx 200$ km s^{-1}. This is in contrast to Schulz et al. (2016), who found the magnitude of any red- or blueshifts to be $\lesssim$200 km s^{-1} but velocity widths on the order of $\lesssim$700 km s^{-1}.

To further compare with the phenomenological models of Schulz et al. (2016), we take the continuum models of Section 3.2 and modify the `tbvarabs` Si edge by either reducing the Si abundance to 0.01 of the ISM value and adding a phenomenological `edge` model (with parameters $E_{\rm edge}$ and $\tau_{\rm edge}$) or allowing the Si abundance ($A_{\rm Si}$) to be a free parameter. These models are referred to as models A and B, respectively, in Table 3, and the flux-corrected spectra[10] in the Si edge region are shown in the top two panels of Figure 5. For both models, the equivalent neutral column is reduced to a value of $N_{\rm H} \approx 4.2 \times 10^{22}$ cm^{-2}, with either the abundance increasing to a value of $A_{\rm Si} = 1.76^{+0.49}_{-0.46}$ or the phenomenological edge requiring an optical depth of $\tau_{\rm edge} = 0.19 \pm 0.05$. Both of these results are completely consistent with those found by Schulz et al. (2016), with the value of the added edge optical depth relative to the fitted equivalent neutral column falling within the data range shown in their Figure 5. The Schulz et al. (2016) results also indicate edge optical depth values approximately twice that predicted by the Wilms et al. (2000) model, consistent with our findings for the fitted abundance in our model B. We note, however, that the magnitude of our fitted value for the equivalent width of the near-edge feature is $\approx$50% larger than the largest values found by Schulz et al. (2016). We further discuss this result below.

Also as discussed by Schulz et al. (2016), the location of the edge has a degree of uncertainty due to the presence of the near-edge absorption feature. In fact, our best-fit edge energy is higher than the absorption feature energy, although the error bars allow for the edge to be at 1.844 keV, which is the expected location for neutral Si at rest.

We next consider a more physical model for the edge region. Specifically, we use the dust-scattering and edge models of Corrales et al. (2016), which, in their `ISIS` implementations,[11] are broken up into individual absorption and scattering components for both silicate and graphite dust grains. We multiply the scattering components by an energy-dependent factor in an identical manner as for the `dustscat` model (Baganoff et al. 2003) to account for the fraction of flux that scatters back into our line of sight given the finite size of the instrumental PSF. We again parameterize this factor with a fixed value of $H_{\rm size} = 200$ (i.e., nearly all scattered photons are lost from the spectrum). We further tie the dust components to the fitted equivalent neutral column via two parameters: the mass fraction of the ISM column in dust ($f_{\rm dust}$) and the fraction of dust in silicates $f_{\rm silicate}$. We fit one model where these values are free parameters (model C) and one model where they are frozen to their commonly presumed values (see Corrales et al. 2016) of $f_{\rm dust} = 0.01$ and $f_{\rm silicate} = 0.6$ (model D). Both models fit the data extremely well, as seen in Figure 5 and Table 3.

We show the fit for model C in Figure 6. The inclusion of scattering and solid-state absorption effects due to dust grains reduces the overall required column to a value of $N_{\rm H} \approx (2.9 \pm 0.5) \times 10^{22}$ cm^{-2}. The presence of a near-edge absorption feature is still required. We note that in terms of equivalent width, all of the models discussed above have comparable values, despite obvious changes in the absolute line depth as seen in Figure 5. This is because the equivalent width

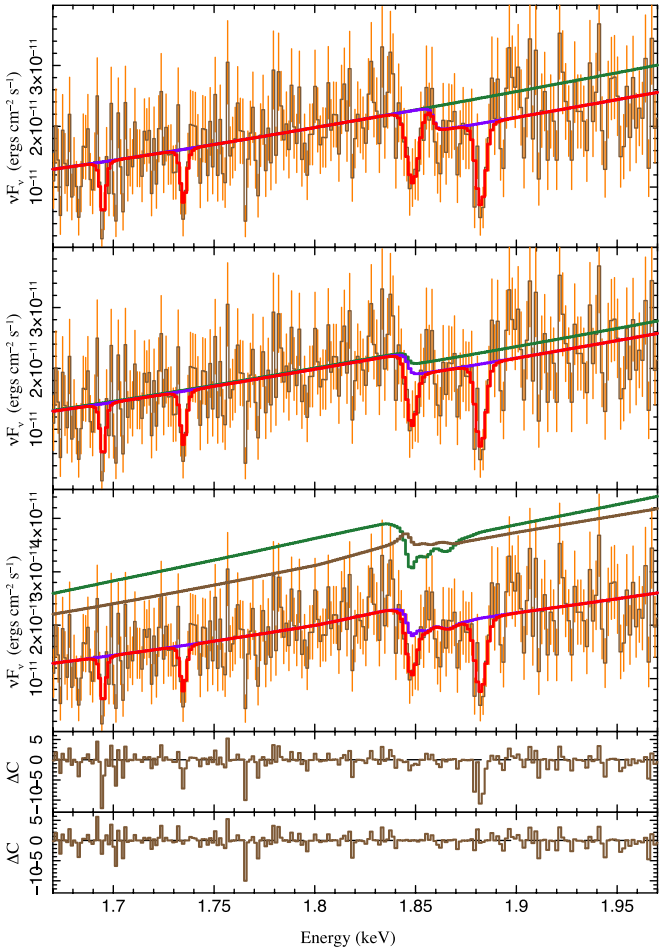

Figure 5. Silicon K-edge region for the flux-corrected combined HEG and MEG first-order *Chandra*-HETG spectra (brown with orange 1σ error bars), fit with an absorbed Comptonized spectrum (see Section 3.2). In all panels, the red line shows the full fitted model, and the purple line shows the model with the absorption lines removed. In the top panel, a phenomenological edge has been used to describe the Si K edge (model A). The green line shows the model with edge and lines removed. In the second panel, the Si K-edge absorption has been modeled by allowing a freely variable (increased) Si abundance in the ISM (model B). The green line shows the model with the Si abundance set to the solar value and the lines removed. The third panel shows the model using the dust-scattering and absorption models of Corrales et al. (2016; model C). The green line shows the model with only the dust absorption contribution. The brown line shows the model with only the dust-scattering contributions. The fourth panel shows the residuals for model C with the lines removed. The fifth panel shows the residuals for model C.

[10] Flux correction is performed on both the model and data counts using the `ISIS` `flux_cor` function, which only relies on the detector response and thus, for the case of the detected counts, is independent of the model.

[11] Available via https://github.com/eblur/ismdust/releases.

Table 2
MCMC Line Significances

Abs	Si Kα	Near Edge	Si XIIIa	Si XIIIb	Si XIIIg	Ca Kα	Ca XIXi	Ca XIXr	Ca XXa
96.9%	66.3%	95.4%	99.999%	64.3%	95.9%	99.4%	99.1%	99.7%	97.0%

Note. Significances from an MCMC analysis of model C, subject to the line constraints discussed in the text. Line identifications are the same in Table 3. Percentages are the fraction of the posterior probability that is <0 for absorption lines and >0 for emission lines. Significances do not include multiplicity of trials.

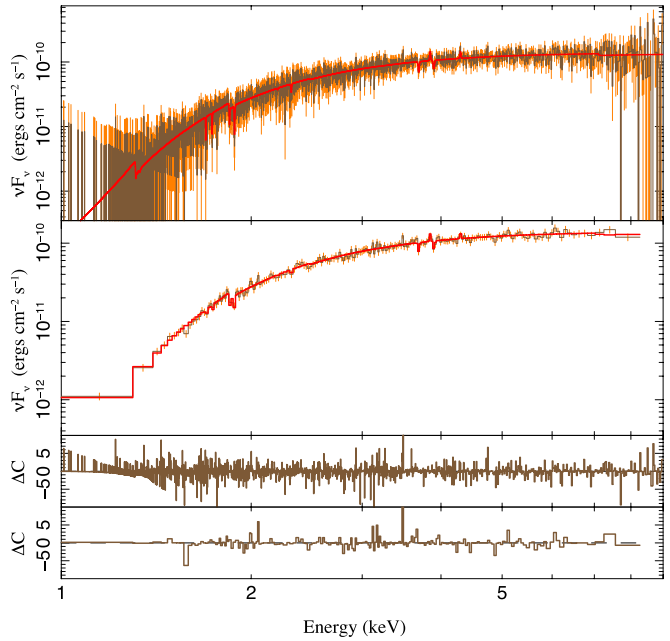

Figure 6. Flux-corrected combined HEG and MEG first-order *Chandra*-HETG spectra (brown with orange 1σ error bars), fit in the 1–9 keV band with an absorbed and scattered Comptonized spectrum (model C; see Section 3.3). Top panel: combined spectrum, with one MEG channel per bin. Second panel: spectrum rebinned to S/N $\geqslant$ 5 and $\geqslant$4 MEG channels per bin, without refitting the spectrum. Third and fourth panels: Cash statistic residuals for the spectral binnings and fit shown in the first two panels.

is a relative measure, and what is being deemed as "continuum" in the equivalent width calculations includes the edge from the absorption/scattering models.

We use model C, which has the most freedom to fit the Si edge region with the neutral absorption and dust-scattering models, to assess the significance of the lines beyond the nominal 90% confidence intervals presented in Table 3. We use this model in an MCMC calculation implemented in `ISIS` following the prescription of Goodman & Weare (2010). (See our detailed descriptions in Murphy & Nowak 2014.) We evolve a set of 320 "walkers" (10 initial models per free parameter, with their initial parameters randomly distributed over the central 3% of the 90% confidence intervals) for 40,000 steps, of which we only retain the last two-thirds for assessing probabilities (yielding over 8.5 million samples in our posterior probability distributions). The line widths and energies are constrained as discussed above.

We calculate line significances as the fraction of the posterior probability distribution with negative line amplitudes for absorption lines or the fraction of the posterior probability distribution with positive amplitudes for emission lines. This is of course a somewhat local and constrained probability distribution that does not account for any "multiplicity of trials" in our initial assessment of lines to include in our models. We present these line significances in Table 2. In general, these significances are commensurate with the results of the 90% confidence intervals presented in Table 3, with the blueshifted Si XIII resonance line being the most significant feature. The Si Kα line is less significant than one might expect from Table 3 owing to the fact that if the line energy shifts from the best-fit value by more than $\approx$5 eV in either direction, a broader weak emission feature is allowed.

3.4. *Joint Fits with* NICER *Spectra*

We next consider models C and D, but with the inclusion of 1–9 keV *NICER* spectra. The *NICER* instrument has a field of view $\approx$30 arcmin^2, i.e., an $\approx$3′ radius (Gendreau et al. 2016). We therefore expect a large fraction of the dust-scattered photons lost from the *Chandra*-HETGS spectra to scatter back into the field of view of *NICER* (see the discussion of Corrales et al. 2016). Although these scattered photons are time-delayed (McCray et al. 1984), there is no indication that the spectrum from tens of thousands of seconds earlier was substantially different from what we observed. As expected, fitting for the size of the dust-scattering halo relative to the *NICER* PSF, we find $H_{\rm size} < 1.9$. (We set the lower bound of $H_{\rm size} = 0.01$.) That is, the spectra are consistent with a substantial fraction (nearly all) of the scattered X-rays returning to the *NICER* field of view. This is in fact apparent when comparing the flux-corrected spectra between *Chandra*-HETGS and *NICER*, as seen in Figure 7.

There are, however, significant residuals for the *NICER* spectra in the $\approx$1.5–2.5 keV region. It is likely that both the fitted equivalent neutral column and the fraction of mass in dust —and, specifically, the fraction of mass in silicate dust—are being partly driven by the systematic uncertainties in the *NICER* response functions. We have used MCMC analyses identically as described above for all of our model fits to determine the interdependencies of the fitted parameters and to make confidence contours of these parameter correlations. Although the contours of the equivalent neutral column versus silicate dust mass column (Figure 8, left) are consistent between *Chandra*-HETGS and *NICER*, the small *NICER* spectra error bars, coupled with large-fit ratio residuals, indicate that *NICER* systematics in this regime are still a significant concern for this aspect of the model fits.

To further bring agreement between the *Chandra*-HETGS and *NICER* spectra, we have to include a cross-normalization between the two detectors. We choose an energy-independent cross-normalization constant, with the only energy-dependent differences between the two observations being the above expected differences due to the dust-scattering halo. Although such energy-dependent cross-calibration differences may exist, we do not believe that these data are sufficiently constraining to allow exploration of a more complicated model. For model E, which allows the greatest freedom in the dust absorption and

Table 3
Spectral Fit Parameters

Parameter	Units	A	B	C	D	E	F
$N_{\rm H}$	10^{22} cm^{-2}	$4.23^{+0.16}_{-0.14}$	$4.21^{+0.18}_{-0.15}$	$2.86^{+0.54}_{-0.55}$	$2.62^{+0.07}_{-0.07}$	$3.28^{+0.10}_{-0.09}$	$2.63^{+0.05}_{-0.21}$
$A_{\rm Si}$		...	$1.76^{+0.48}_{-0.47}$	...	...	...	...
$E_{\rm edge}$	keV	$1.859^{+0.004}_{-0.020}$	...	...	...	...	...
$\tau_{\rm edge}$		$0.19^{+0.05}_{-0.05}$	...	...	...	...	...
$f_{\rm dust}$	10^{-2}	...	...	$0.71^{+0.60}_{-0.26}$	*1*	$0.49^{+0.04}_{-0.04}$	*1*
$f_{\rm silicate}$		...	...	$0.92^{+0.08}_{-0.49}$	*0.6*	$1.0_{-0.06}$	*0.6*
$C_{\rm n}$		...	...	...	...	$0.83^{+0.02}_{-0.02}$	$0.77^{+0.01}_{-0.01}$
$H_{\rm size}$		...	...	...	...	$0.01^{+1.33}_{-0.0}$	$1.85^{+0.06}_{-0.06}$
$N_{\rm nc}$		$0.09^{+0.01}_{-0.01}$	$0.09^{+0.01}_{-0.01}$	$0.10^{+0.02}_{-0.01}$	$0.10^{+0.01}_{-0.01}$	$0.10^{+0.01}_{-0.01}$	$0.09^{+0.01}_{-0.01}$
$\Gamma_{\rm nc}$		$1.98^{+0.06}_{-0.07}$	$1.99^{+0.07}_{-0.07}$	$2.06^{+0.08}_{-0.07}$	$2.05^{+0.05}_{-0.05}$	$2.02^{+0.04}_{-0.02}$	$1.96^{+0.03}_{-0.03}$
$kT_{\rm nc}$	keV	$0.084^{+0.003}_{-0.003}$	$0.082^{+0.003}_{-0.002}$	*0.06*	*0.06*	$0.057^{+0.001}_{-0.001}$	$0.074^{+0.002}_{-0.007}$
$N_{\rm bb}$	10^7	$5.5^{+1230}_{-5.2}$	$8.1^{+630}_{-7.7}$	330^{+470}_{-270}	400^{+390}_{-290}	2000^{+3800}_{-1900}	$30.7^{+230}_{-22.2}$
$E_{\rm abs}$	keV	$1.6949^{+0.0005}_{-0.0008}$	$1.6949^{+0.0006}_{-0.0008}$	$1.6949^{+0.0005}_{-0.0008}$	$1.6949^{+0.0006}_{-0.0008}$	*1.6949*	*1.6949*
$\sigma_{\rm abs}$	eV	$0.2^{+0.9}_{-0.1}$	$0.2^{+0.9}_{-0.1}$	$0.2^{+0.9}_{-0.1}$	$0.2^{+0.9}_{-0.1}$	*0.2*	*0.2*
EW$_{\rm abs}$	eV	$-2.3^{+1.1}_{-0.8}$	$-2.3^{+0.9}_{-0.8}$	$-2.3^{+0.6}_{-1.2}$	$-2.3^{+0.9}_{-0.8}$	*−2.3*	*−2.3*
$E_{\rm Si\ K\alpha}$	keV	$1.735^{+0.001}_{-0.001}$	$1.735^{+0.001}_{-0.001}$	$1.735^{+0.001}_{-0.001}$	$1.735^{+0.001}_{-0.001}$	*1.735*	*1.735*
$\sigma_{\rm Si\ K\alpha}$	eV	$0.2^{+1.3}_{-0.1}$	$0.3^{+1.1}_{-0.2}$	$0.2^{+1.3}_{-0.1}$	$0.2^{+1.3}_{-0.1}$	*0.2*	*0.2*
EW$_{\rm Si\ K\alpha}$	eV	$-2.3^{+1.1}_{-0.8}$	$-2.3^{+1.2}_{-0.8}$	$-2.2^{+0.4}_{-0.9}$	$-2.3^{+1.2}_{-0.8}$	*−2.2*	*−2.3*
$E_{\rm near\ edge}$	keV	$1.848^{+0.002}_{-0.001}$	$1.848^{+0.002}_{-0.002}$	$1.848^{+0.002}_{-0.003}$	$1.848^{+0.002}_{-0.002}$	*1.848*	*1.848*
$\sigma_{\rm near\ edge}$	eV	$2.1^{+2.1}_{-2.0}$	$1.6^{+2.6}_{-1.5}$	$1.8^{+3.0}_{-1.7}$	$1.8^{+2.9}_{-1.7}$	*1.8*	*1.8*
EW$_{\rm near\ edge}$	eV	$-4.1^{+2.0}_{-1.7}$	$-3.3^{+1.5}_{-2.0}$	$-3.3^{+2.2}_{-0.5}$	$-3.3^{+2.4}_{-0.1}$	*−3.3*	*−3.3*
$z_{\rm Si\ XIII}$		$0.0093^{+0.0006}_{-0.0009}$	$0.0093^{+0.0006}_{-0.0010}$	$0.0092^{+0.0007}_{-0.0008}$	$0.0092^{+0.0006}_{-0.0008}$	*0.0092*	*0.0092*
$\sigma_{\rm Si\ XIII}$	eV	$1.5^{+2.2}_{-1.2}$	$1.5^{+2.3}_{-1.2}$	$1.7^{+1.8}_{-1.4}$	$1.8^{+1.9}_{-1.5}$	*1.8*	*1.8*
EW$_{\rm Si\ XIIIa}$	eV	$-4.3^{+0.7}_{-1.7}$	$-4.4^{+1.5}_{-1.8}$	$-4.7^{+1.8}_{-1.5}$	$-4.7^{+1.8}_{-1.6}$	*−4.7*	*−4.7*
EW$_{\rm Si\ XIIIb}$	eV	$-0.7^{+2.9}_{-2.1}$	$-0.6^{+2.8}_{-2.1}$	$-0.5^{+2.9}_{-2.0}$	$-0.5^{+2.9}_{-2.2}$	*−0.5*	*−0.5*
EW$_{\rm Si\ XIIIg}$	eV	$-2.3^{+2.9}_{-3.3}$	$-2.3^{+2.9}_{-3.3}$	$-2.4^{+3.1}_{-3.0}$	$-2.4^{+2.6}_{-3.1}$	*−2.4*	*−2.4*
$E_{\rm Ca\ K\alpha}$	keV	$3.687^{+0.007}_{-0.006}$	$3.687^{+0.007}_{-0.007}$	$3.687^{+0.007}_{-0.006}$	$3.687^{+0.007}_{-0.006}$	*3.687*	*3.687*
$\sigma_{\rm Ca\ K\alpha}$	eV	$4.3^{+7.8}_{-4.2}$	$4.3^{+7.8}_{-4.2}$	$4.4^{+7.8}_{-4.3}$	$4.3^{+7.8}_{-4.2}$	*4.4*	*4.3*
EW$_{\rm Ca\ K\alpha}$	eV	$-6.1^{+3.2}_{-3.2}$	$-6.1^{+3.2}_{-3.2}$	$-6.2^{+3.8}_{-3.3}$	$-6.1^{+3.2}_{-3.2}$	*−6.2*	*−6.1*
$E_{\rm Ca\ XIXi}$	keV	$3.845^{+0.028}_{-0.014}$	$3.845^{+0.027}_{-0.014}$	$3.845^{+0.029}_{-0.015}$	$3.845^{+0.027}_{-0.014}$	*3.845*	*3.845*
$\sigma_{\rm Ca\ XIXi}$	eV	$0.7^{+19.3}_{-0.6}$	$1.1^{+18.9}_{-1.0}$	$1.0^{+19.0}_{-0.9}$	$0.6^{+19.4}_{-0.5}$	*1.0*	*0.6*
EW$_{\rm Ca\ XIXi}$	eV	$6.1^{+15.8}_{-3.5}$	$6.1^{+15.5}_{-3.5}$	$6.0^{+61.6}_{-3.6}$	$6.1^{+29.2}_{-3.6}$	*6.0*	*6.1*
$E_{\rm Ca\ XIXr}$	keV	$3.896^{+0.011}_{-0.008}$	$3.896^{+0.011}_{-0.008}$	$3.896^{+0.011}_{-0.008}$	$3.896^{+0.011}_{-0.008}$	*3.896*	*3.896*
$\sigma_{\rm Ca\ XIXr}$	eV	$6.4^{+12.8}_{-6.3}$	$6.4^{+12.9}_{-6.3}$	$6.5^{+13.0}_{-6.4}$	$6.4^{+12.9}_{-6.3}$	*6.5*	*6.4*
EW$_{\rm Ca\ XIXr}$	eV	$-6.6^{+3.9}_{-4.4}$	$-6.6^{+3.9}_{-4.5}$	$-6.7^{+4.0}_{-4.4}$	$-6.6^{+3.9}_{-4.2}$	*−6.7*	*−6.6*
$E_{\rm Ca\ XXa}$	keV	$4.295^{+0.007}_{-0.010}$	$4.295^{+0.006}_{-0.009}$	$4.294^{+0.007}_{-0.006}$	$4.296^{+0.005}_{-0.011}$	*4.294*	*4.294*
$\sigma_{\rm Ca\ XXa}$	eV	$0.8^{+1.3}_{-0.7}$	$0.2^{+0.0}_{-0.1}$	$0.3^{+2.7}_{-0.2}$	$0.3^{+0.2}_{-0.2}$	*0.5*	*0.3*
EW$_{\rm Ca\ XXa}$	eV	$7.0^{+5.3}_{-4.3}$	$6.9^{+5.2}_{-4.2}$	$6.9^{+1.1}_{-4.5}$	$6.8^{+0.9}_{-4.2}$	*6.9*	*6.8*
Cash/dof		1958.7/2170	1959.6/2171	1956.6/2171	1957.8/2173	2507.0/2645	2597.1/2647

Note. All errors are at the 90% confidence level for one interesting parameter (determined as ΔCash = 2.71, which is correct in the limit that Cash statistics approach χ^2 statistics). Models A–D are for *Chandra*-HETG 1–9 keV spectra only, while models E and F also include *NICER* 1–9 keV spectra. Italicized parameters were held fixed at that value. See text for a description of the models and model parameters.

scattering parameters, we also find the largest cross-normalization constant, 0.83 ± 0.02. This is somewhat lower than one might initially expect from the 1–9 keV *NICER* flux, which is 1.48×10^{-10} erg cm^{-2} s^{-1}(see Figure 1). Note, however, that the *NICER* spectra are less affected by the dust halo and therefore would have a slightly higher flux than *Chandra*-HETGS, even if the cross-normalization constant were unity.

In Figure 8, we show the dependence of this cross-normalization constant on the fitted and/or presumed equivalent neutral and silicate dust mass columns. There are significant systematic dependencies upon the latter, which is not surprising, given the ratio residuals present in Figure 7. For the models that we have explored, however, we have not found a cross-normalization constant $\gtrsim$0.85.

4. Discussion

We have presented a series of fits to *INTEGRAL*, *NICER*, and *Chandra*-HETGS spectra of the AMXP IGR J17591−2342, together with on-source NIR observations performed within our collaboration.

4.1. Comparison with Previous Findings

Our IBIS/ISGRI spectrum of the brightest part of the hard X-ray outburst of IGR J17591−2342 (24 ks; Figure 2) results in a nonattenuated power-law model ($\Gamma = 2.0 \pm 0.2$) with no cutoff required and source detection up to about 110 keV. This is compatible with what was found in the dedicated *INTEGRAL* target-of-opportunity observations of the source (164 ks;

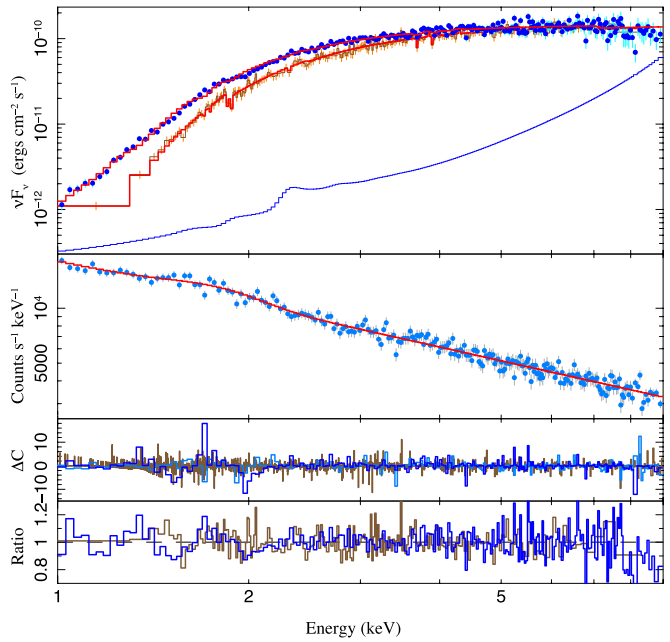

Figure 7. Top panel: flux-corrected combined HEG and MEG first-order *Chandra*-HETG spectra (brown histogram) and *NICER* spectra (blue circles; the pale blue histogram is the background model), jointly fit with an absorbed and scattered blackbody-plus-Comptonization model (model E). Owing to the different fields of view of each instrument, the dust-scattering component is different in the *Chandra* and *NICER* spectra and accounts for the deviation between the two spectra at energies $\lesssim$3 keV. The *NICER* spectra also have been renormalized to account for a fitted cross-normalization constant between the *Chandra*-HETGS and *NICER* spectra. The second panel shows the simultaneous fit to the background spectra (see text). The third and fourth panels show the residuals for the model fit. The third panel shows the Cash statistics residuals for the *Chandra*-HETGS (brown histogram) and *NICER* source (blue histogram) and background (light blue histogram) spectra at the binning of the fit (see text). The fourth panel shows the the data/model ratio residuals, now omitting the *NICER* background spectra and with the *Chandra*-HETGS spectra rebinned for clarity but without refitting the model.

Kuiper et al. 2018) that significantly detected IGR J17591−2342 up to 150 keV using a power-law model description. Such a high-energy spectrum is representative for AMXPs that are known to have quite high Comptonizing plasma temperatures of the order of several tens of keV (e.g., Falanga et al. 2013 and references therein), similar to the so-called Atoll LMXBs known to host NSs.

In agreement with the many preliminary analyses presented in the references of Section 1, and specifically with the *Swift*/*NICER*/*NuSTAR*/*INTEGRAL* analyses presented by Sanna et al. (2018), we find that a highly absorbed power law ($N_{\rm H} \approx 4 \times 10^{22}$ cm^{-2}, $\Gamma \approx 2$) describes the spectra well. When specifically modeling the 1–9 keV spectra with a Comptonized blackbody, fixing the coronal temperature to the 22 keV employed by Sanna et al. (2018), there is an implied spectral curvature in the 50–150 keV *INTEGRAL* band that we do not detect. However, our 1–9 keV spectra are largely insensitive to the temperature of the corona and instead are predominantly sensitive to the spectral slope of the Compton continuum, which is $\Gamma \approx 2$ for all of the models that we have considered.

Our one major difference from the models of Sanna et al. (2018) is that we fit a lower temperature, and hence a larger normalization, for the seed photons input to the Compton corona. They found a blackbody emission area consistent with the surface of an NS. In contrast, the blackbody normalizations presented in Table 3 imply emission radii ranging from ≈1000 to 200,000 km if the source is at the 8 kpc distance of the Galactic bulge. This would imply that the seed photons for Comptonization were instead generated by the accretion flow onto the NS, rather than its surface.

A second difference between our model fit results and previous fit results using spectra from detectors with lower spectral resolution than that for *Chandra*-HETGS concerns the fitted equivalent neutral column. Our model fits to $N_{\rm H}$ are driven not only by the curvature of the soft X-ray continuum spectra but also by direct modeling of X-ray absorption edges of various atomic species. The advent of the era of high-resolution spectroscopy is among the factors that drove the development of the `tbvarabs` model (Wilms et al. 2000). This model utilizes improved knowledge of ISM abundances and atomic cross sections, and it also provides a more precise description of atomic edges from such species as O, Fe (via the L and K edges), Ne, and, for the case of IGR J17591−2342, the Si edge. However, as pointed out by Schulz et al. (2016), the `tbvarabs` model underpredicts the depth of the Si edge for a given equivalent neutral column. Phenomenologically, this can be accounted for by either adding a separate Si-region edge to the model (while artificially reducing the Si abundance) with $\tau_{\rm edge} = 0.19 \pm 0.05$ or increasing the Si abundance in the model to $A_{\rm Si} = 1.76^{+0.48}_{-0.47}$ (models A and B in Table 3). This is in complete agreement with the results of Schulz et al. (2016) and also with newer abundance measurements for B stars in the Galaxy (Nieva & Przybilla 2012), which imply $A_{\rm Si} = 1.70$.

4.2. Dust Absorption/Scattering and Source Distance

A more physical description of this result is provided by employing the models of Corrales et al. (2016). As pointed out by these authors, as an absorption model, the `tbvarabs` model does not account for soft X-ray scattering or solid-state absorption effects by dust except for shielding. Both are important for the high spatial resolution observations of *Chandra*-HETGS. Dust scatters X-rays out of our line of sight on arcsecond-sized scales, but it scatters back into the line of sight, albeit with a time delay, on arcminute scales (McCray et al. 1984). Thus, we have to account for both dust-scattering and solid-state absorption effects in modeling the *Chandra*-HETGS spectra of IGR J17591−2342. We have done this in models C and D from Table 3 using the dust models of Corrales et al. (2016). The inclusion of dust has the effect of reducing the required equivalent neutral column. Since it contains the least restrictive assumptions about the column mass fraction in dust or the fraction of dust in silicates, we consider model C, with $N_{\rm H} = (2.9 \pm 0.5) \times 10^{22}$ cm^{-2}, to be our fairest estimate for the equivalent neutral column[12] along our line of sight to IGR J17591−2342.

This value is lower, by ≈1/5–1/3, compared to model estimates made without accounting for dust effects (e.g., Russell et al. 2018b; Sanna et al. 2018). As discussed by Russell et al. (2018b), the equivalent neutral column inferred from reddening maps is $N_{\rm H} < 2.2 \times 10^{22}$ cm^{-2} (for the full column along the line of sight), and it is $N_{\rm H} > 0.7 \times 10^{22}$ cm^{-2} for distances

[12] Again using the Predehl & Schmitt (1995) and Fitzpatrick (1999) relationships between extinction and equivalent column, this implies *I*- and *K*-band absorptions of $A_V = 16.2$ and $A_K = 1.85$ mag. Both absorptions are high and still consistent with a nondetection in the *I* band, as discussed in Section 2.4.

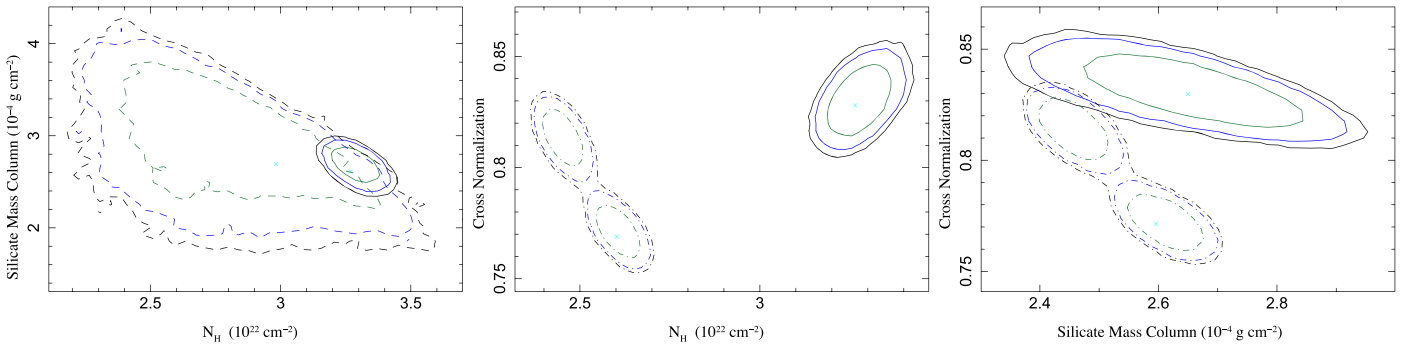

Figure 8. Contours for interstellar and dust absorption and scattering parameters for absorbed/scattered blackbody-plus-Comptonization fits to the 1–9 keV *Chandra*-HETG spectra on their own (dashed contours, model C) or in combination with the 1–9 keV *NICER* spectrum (solid contours, model E; dash-dotted contours, model F), as derived from MCMC analyses of the model fits. Left: equivalent hydrogen column for gas absorption versus silicate mass column for dust scattering and absorption. Middle: cross-normalization value for the *NICER* spectrum (relative to *Chandra*-HETG normalization) versus equivalent hydrogen column. Solid contours are for a freely variable dust mass and silicate fraction (see Section 3.3), while the dash-dotted contours presume a fixed dust mass fraction of 0.01 and a fixed silicate fraction of 0.6. Right: *NICER* cross-normalization constant versus silicate mass column for both freely variable and fixed dust mass and silicate fractions.

>6 kpc. Thus, Russell et al. (2018b) argued for a large distance, at the Galactic bulge distance or beyond, and further argued that IGR J17591−2342 is radio-bright for an AMXP. (In fact, based upon its radio brightness relative to its X-ray flux, IGR J17591−2342 was initially hypothesized to be a black hole candidate; Russell et al. 2018a.) Russell et al. (2018b) offered the alternative hypothesis that if much of the absorption is local to the system, then it can be significantly closer, allowing for a more typical ratio of radio to X-ray luminosity for an AMXP. (Empirically, the radio flux drops more slowly than the X-ray flux for decreasing luminosities.)

Although our inclusion of the dust effects lowers the fitted equivalent neutral column, it does not do so substantially enough to fundamentally alter the conclusions[13] of Russell et al. (2018b).

A further argument in favor of the source being at a large distance with a column primarily attributable to the ISM (as opposed to local absorption) is the presence of a substantial near-edge absorption feature at an energy of 1.848 keV. Such a near-edge absorption feature is routinely seen in X-ray binary sources with columns in the range of ≈(1–8) × 10^{22} cm^{-2} (Schulz et al. 2016); however, the near-edge feature is often variable and of lower equivalent width magnitude than we observe here. The speculation is that dust local to the system is destroyed/ionized by the source's X-rays. Schulz et al. (2016) essentially fit a spectral model equivalent to model A in Table 3, and the highest-magnitude equivalent widths they found are ≈−8 ± 2 mA for $N_H \gtrsim 4 \times 10^{22}$ cm^{-2}. For IGR J17591−2342 fit with model A, we find EW = $-4.1^{+2.0}_{-1.7}$ eV = -16^{+8}_{-7} mA. If this feature were primarily local and subject to destruction by ionization due to the source, it would be unusual to find its equivalent width at a magnitude greater than that observed in the entire Schulz et al. (2016) sample while at the same time also seeing an Si XIII absorption line with a high-magnitude equivalent width (EW = $-4.3^{+0.7}_{-1.7}$ eV, =-15^{+3}_{-6} mA for model A) outflowing at 0.0093 c, where c is the speed of light. Thus, we hypothesize that a large fraction of the observed column is associated with the ISM (as is consistent with our NIR results, discussed in Section 2.4), the source is at a large distance, and, hence, its radio flux is indeed high for an AMXP.

[13] It should be noted that "equivalent neutral column" is often used as a proxy parameter; however, it is not always clear within the literature to what degree this parameter is the same for different types of measurements. That is, what are the systematic differences between this parameter when discussing X-ray absorption versus X-ray dust halos versus interstellar reddening versus 21 cm measurements? Discussing the potential systematic differences for the equivalent neutral column used in each type of measurement is well beyond the scope of this work. However, this does not alter the basic conclusion that our measured column would have to be predominantly local to the source in order to have IGR J17591−2342 be substantially closer than the Galactic bulge distance.

4.3. Outflowing Wind

The Si XIII absorption line indicates a mass outflow in the IGR J17591−2342 system. We can constrain the energy flux associated with this outflow based upon the line equivalent width. Assuming that the line is on the linear part of the curve of growth, W_λ, its equivalent width in Å is related to the Si XIII column, $N_{\rm Si13}$, by

$$\frac{W_\lambda}{\lambda} = \frac{\pi e^2}{m_e c^2} N_{\rm Si13}\, \lambda\, f_{\rm ij} = (8.85 \times 10^{-13}\ {\rm cm})\, N_{\rm Si13}\, \lambda\, f_{\rm ij} \quad (2)$$

(Spitzer 1978). Using an oscillator strength of 0.75 (Kramida et al. 2018), the column is $N_{\rm Si13} = 5 \times 10^{16}$ cm^{-2}, which yields a wind kinetic energy flux of

$$E_{\rm wind} = 2 \times 10^{13} \left(\frac{f_{\rm Si13}}{0.1}\right)^{-1} {\rm erg\ cm^{-2}\ s^{-1}}, \quad (3)$$

where $f_{\rm Si13}$ is the fraction of Si in Si XIII, and we have used the ISM abundances of Wilms et al. (2000) in going from an Si column to a hydrogen column.

In order to determine the total kinetic energy luminosity, we would need to know the characteristic wind radius. The large effective radius of the blackbody seed photons suggests a large wind launching radius, $\gtrsim 10^{10}$ cm. The narrow width of the Si XIII line suggests an even larger radius, $\gtrsim 10^{11}$ cm. The kinetic energy luminosity of the wind then becomes

$$E_{\rm wind} = 2 \times 10^{35} \left(\frac{f_{\rm Si13}}{0.1}\right)^{-1} \left(\frac{\Omega_{\rm wind}}{4\pi}\right) \left(\frac{R_{\rm wind}}{10^{11}\ {\rm cm}}\right) {\rm erg\ s^{-1}}, \quad (4)$$

where $\Omega_{\rm wind}$ is the solid angle subtended by the wind and $R_{\rm wind}$ is the wind launching radius. This is potentially a large fraction of the luminous energy of the source.

Of the additional lines that we included in our models, the only plausible identifications that we have are with various species of Ca. These are not at a consistent set of velocity shifts or even all in emission or absorption. If the line identifications

are real, these lines could be associated with a variety of locations in the accretion flow and/or the atmosphere of the companion star and may indicate an overabundance of calcium in the system. It is possible that the progenitor of the IGR J17591−2342 system was the collapse of a white dwarf, producing a calcium-rich Type Ib supernova (Perets et al. 2010; see also Canal et al. 1990; Metzger et al. 2009); one possible example of such a system comes from optical/*Chandra* observations of an NS binary system with a calcium overabundance of a factor of 6 within the supernova remnant RCW 86 that likely will evolve into an LMXB system (Gvaramadze et al. 2017). It may be that IGR J17591−2342 is a later evolutionary stage of such a system.

Theoretical scenarios show a clear variety of evolutionary channels in LMXBs, and it is not easy to estimate the presence/amount of Ca therein, especially when subject to long-term (possibly intermittent) X-ray irradiation that dramatically alters the evolution of the system, be it by irradiation-driven winds and/or expansion of the companion (e.g., Podsiadlowski et al. 2002; Nelson & Rappaport 2003; Tauris & van den Heuvel 2006). However, highly ionized atmospheres or winds are known to be present in LMXBs and are detected as warm emitters and/or absorbers in many systems (Díaz Trigo & Boirin 2016 and references therein). Some Ca XX absorption lines have been detected in the *XMM-Newton* spectra of GX 13+1 (Sidoli et al. 2002; Ueda et al. 2004), as well as in MXB 1659−298 (Ponti et al. 2018). Similarly, the presence of Ca has been observed in the AMXP SAX J1748.9−2021 (Pintore et al. 2016), as well as in the binary millisecond pulsar PSR J1740−5340 (Sabbi et al. 2003). These findings, together with our results on IGR J17591−2342, seem to suggest that the accretion flow and/or companion atmosphere can be Ca-rich if the companion is subject to prolonged mass loss and interactions with the millisecond pulsar.

4.4. A Multifacility Approach: Final Considerations

Similarly to the so-called Atoll LMXBs known to host NSs, AMXPs are known to have X-ray spectra characterized by high Comptonizing plasma temperatures of the order of several tens of keV (e.g., Falanga et al. 2013 and references therin). This results in nonattenuated power-law spectra up to hundreds of keV, compatible with what we found for the brightest part of the outburst.

On the lower-energy part of the spectrum, we note that there is overall good agreement between the *Chandra*-HETGS and *NICER* 1–9 keV spectra if one carefully accounts for the manner in which each instrument views the scattering by the dust halo in front of IGR J17591−2342. The differences seen between the two flux-corrected spectra in Figure 7 are primarily due to the effects of dust scattering, rather than uncertainties in instrumental response. As regards the instrumental response, essentially all of our detailed information regarding absorption and outflows in the IGR J17591−2342 system comes from the high-resolution HETGS. *NICER* lacks the spectral resolution and currently has significant response uncertainties in the $\approx$2 keV region. There also remains an $\gtrsim$15% normalization difference between the *Chandra*-HETGS and *NICER* spectra (Figure 8). On the other hand, *Chandra*-HETGS is incapable of achieving the time resolution of *NICER* that was required to characterize the pulsar and orbital periods of the IGR J17591−2342 system (see Sanna et al. 2018).

Together, these instruments, along with the radio and NIR measurements discussed above, paint a picture of IGR J17591−2342 as a somewhat distant system with a high-velocity outflow and an unusually bright radio flux for an AMXP that might have formed from a rare, calcium-rich supernova explosion.

The authors thank Lia Corrales for useful discussions concerning dust scattering and members of the *NICER* team, especially Paul Ray, for discussions concerning the *NICER* spectra. M.A.N. gratefully acknowledges funding support from the National Aeronautics and Space Administration through *Chandra* Guest Observer grant GO8-19022X. A.P. acknowledges financial contribution from ASI/INAF contract No. 2013-025.R1 and ASI-INAF agreement No. 2017-14-H.0. J.R. acknowledges partial funding from the French Space Agency (CNES). S.C. and F.F. are grateful to the Centre National d'Etudes Spatiales (CNES) for the funding of the Multi-wavelength *INTEGRAL* Network (MINE). G.K.J. acknowledges support from Marie Skłodowska-Curie Actions grant No. 713683 (H2020; COFUNDPostdocDTU). Based on observations with *INTEGRAL*, an ESA project with instruments and a science data center funded by ESA member states (especially the PI countries: Denmark, France, Germany, Italy, Spain, and Switzerland), the Czech Republic, and Poland and with the participation of Russia and the USA. Based on observations collected at the European Organisation for Astronomical Research in the Southern Hemisphere under ESO program(s) 0101.D-0082(A).

Facilities: CXO (ACIS, HETG), *INTEGRAL*, *NICER*, *Swift* (XRT), ESO, VLT (HAWK-I).

Software: XSPEC, ISIS.

ORCID iDs

Michael A. Nowak https://orcid.org/0000-0001-6923-1315
Adamantia Paizis https://orcid.org/0000-0001-5067-0377
Gaurava Kumar Jaisawal https://orcid.org/0000-0002-6789-2723
Jérôme Chenevez https://orcid.org/0000-0002-4397-8370
Sylvain Chaty https://orcid.org/0000-0002-5769-8601
Francis Fortin https://orcid.org/0000-0003-3642-2267
Jérôme Rodriguez https://orcid.org/0000-0002-4151-4468
Jörn Wilms https://orcid.org/0000-0003-2065-5410

References

Alpar, M. A., Cheng, A. F., Ruderman, M. A., & Shaham, J. 1982, Natur, 300, 728
Arnaud, K. A. 1996, in ASP Conf. Ser. 101, Astronomical Data Analysis Software and Systems V, ed. J. H. Jacoby & J. Barnes (San Francisco, CA: ASP), 17
Baganoff, F. K., Maeda, Y., Morris, M., et al. 2003, ApJ, 591, 891
Bozzo, E., Ducci, L., Ferrigno, C., et al. 2018, ATel, 11942
Campana, S., & Di Salvo, T. 2018, in The Physics and Astrophysics of Neutron Stars, ed. L. Rezzolla et al. (Berlin: Springer)
Canal, R., Isern, J., & Labay, J. 1990, ARA&A, 28, 183
Canizares, C. R., Davis, J. E., Dewey, D., et al. 2005, PASP, 117, 1144
Cash, W. 1979, ApJ, 228, 939
Corrales, L. R., García, J., Wilms, J., & Baganoff, F. 2016, MNRAS, 458, 1345
Davis, J. E. 2001, ApJ, 548, 1010
Díaz Trigo, M., & Boirin, L. 2016, AN, 337, 368
Ducci, L., Kuulkers, E., Grinberg, V., et al. 2018, ATel, 11941
Falanga, M., Kuiper, L., Poutanen, J., et al. 2013, Proc. "An INTEGRAL view of the high-energy sky (the first 10 years)", arXiv:1302.2843
Ferrigno, C., Bozzo, E., Sanna, A., et al. 2018, ATel, 11957
Fitzpatrick, E. L. 1999, PASP, 111, 63
Freudling, W., Romaniello, M., Bramich, D. M., et al. 2013, A&A, 559, A96

Gendreau, K. C., Arzoumanian, Z., Adkins, P. W., et al. 2016, Proc. SPIE, 9905, 99051
Goodman, J., & Weare, J. 2010, CAMCS, 5, 65
Gvaramadze, V. V., Langer, N., Fossati, L., et al. 2017, NatAs, 1, 0116
Hanke, M., Wilms, J., Nowak, M. A., et al. 2009, ApJ, 690, 330
Hell, N., Brown, G. V., Wilms, J., et al. 2016, ApJ, 830, 26
Houck, J. C., & Denicola, L. A. 2000, in ASP Conf. Ser. 216, Astronomical Data Analysis Software and Systems IX (San Francisco, CA: ASP), 591
Huenemoerder, D. P., Mitschang, A., Dewey, D., et al. 2011, AJ, 141, 129
Jahoda, K., Swank, J. H., Giles, A. B., et al. 1996, Proc. SPIE, 2808, 59
Jaisawal, G. K., Naik, S., Gupta, S., Chenevez, J., & Epili, P. 2018, MNRAS, 478, 448
Kramida, A., Ralchenko, Y., Reader, J. & NIST ASD Team 2018, NIST Atomic Spectra Database (ver. 5.2), [2018 October 24] (National Institute of Standards and Technology: Gaithersburg,MD) Available: http://physics.nist.gov/asd
Krimm, H. A., Barthelmy, S. D., Cummings, J. R., et al. 2018, ATel, 11985
Kuiper, L., Tsygankov, S., Falanga, M., et al. 2018, ATel, 12004
Lebrun, F., Leray, J. P., Lavocat, P., et al. 2003, A&A, 411, L141
Lund, N., Budtz-Jørgensen, C., Westergaard, N. J., et al. 2003, A&A, 411, L231
McCray, R., Kallman, T. R., Castor, J. I., & Olson, G. L. 1984, ApJ, 282, 245
Metzger, B. D., Piro, A. L., & Quataert, E. 2009, MNRAS, 396, 1659
Murphy, K. D., & Nowak, M. A. 2014, ApJ, 797, 11
Nelson, L. A., & Rappaport, S. 2003, ApJ, 598, 431
Nieva, M.-F., & Przybilla, N. 2012, A&A, 539, A143
Nowak, M., Paizis, A., Chenevez, J., et al. 2018, ATel, 11988
Nowak, M. A. 2017, AN, 338, 227
Nowak, M. A., Neilsen, J., Markoff, S. B., et al. 2012, ApJ, 759, 95
Papitto, A. 2016, MmSAI, 87, 543
Patruno, A., & Watts, A. L. 2012, arXiv:1206.2727
Perets, H. B., Gal-Yam, A., Mazzali, P. A., et al. 2010, Natur, 465, 322
Pintore, G., Sanna, A., DiSalvo, T., et al. 2016, MNRAS, 457, 2988
Podsiadlowski, P., Rappaport, S., & Pfahl, E. D. 2002, A&A, 385, 940
Ponti, G., Bianchi, S., Muñoz-Darias, T., & Nandra, K. 2018, MNRAS, 481, L94
Predehl, P., & Schmitt, J. H. M. M. 1995, A&A, 293, 889
Russell, D. M., Degenaar, R., & van den Eijnden, J. 2018a, ATel, 11954
Russell, D. M., & Lewis, F. 2018, ATel, 11946
Russell, T. D., Degenaar, N., Wijnands, R., et al. 2018b, ApJ, 869, L16
Sabbi, E., Gratton, R. G., Bragaglia, A., et al. 2003, A&A, 412, 829
Sanchez-Fernandez, C., Ferrigno, C., Chenevez, J., et al. 2018, ATel, 12000
Sanna, A., Ferrigno, C., Ray, P. S., et al. 2018, A&A, 617, L8
Schulz, N. S., Corrales, L., & Canizares, C. R. 2016, ApJ, 827, 49
Shaw, A. W., Degenaar, N., & Heinke, C. O. 2018, ATel, 11970
Sidoli, L., Parmar, A. N., Oosterbroek, T., & Lumb, D. 2002, A&A, 385, 940
Spitzer, L. 1978, Physical processes in the interstellar medium (New York: Wiley & Sons)
Tauris, T. M., & van den Heuvel, E. P. J. 2006, in Compact Stellar X-ray Source, ed. W. H. G. Lewin & M. van der Klis (Cambridge: Cambridge Univ. Press)
Tudor, V., Miller-Jones, J. C. A., Patruno, A., et al. 2017, MNRAS, 470, 324
Ueda, Y., Murakami, H., Yamaoka, K., Dotani, T., & Ebisawa, K. 2004, ApJ, 609, 325
Vernet, J., Dekker, H., D'Odorico, S., et al. 2011, A&A, 536, 105
Weisskopf, M. C., Brinkman, B., Canizares, C., et al. 2002, PASP, 114, 1
Wilms, J., Allen, A., & McCray, R. 2000, ApJ, 542, 914
Winkler, C., Courvoisier, T. J.-L., Di Cocco, G., et al. 2003, A&A, 411, L1
Winkler, C., Diehl, R., Ubertini, P., & Wilms, J. 2011, SSRv, 161, 149
Życki, P. T., Done, C., & Smith, D. A. 1999, MNRAS, 309, 561